AIAA SCITECH 2024 Forum, 8-12 January 2024, Orlando, USA. AIAA 2024-2723
DOI:10.2514/6.2024-2723

CFD study of Shock Bump Roughness for Transonic Shock Control and Buffet Alleviation

T. Desai * , D. Di Pasquale† , S. Prince.‡
SATM, Centre for Aeronautics, Cranfield University, College Road, Cranfield, Bedfordshire MK43 0AL, UK

M. Chotard§
Safran AE, Théhillac, Brittany, France

Shock induced separation is a serious problem in the transonic flow regime which leads to buffet - unsteady aerodynamic loading on the wing, that can cause serious structural fatigue and failure. These phenomena compromise the flight envelope and structural integrity of an aircraft, and consequently its operational safety. One possible solution is to control and delay the boundary layer separation. The aim of this work was to numerically study whether sub-boundary layer scale distributed roughness, arranged in periodic strips, which locally increases the boundary layer displacement thickness, can act as a virtual shock bump with the aim of bifurcating the foot of the shock wave to reduce the shock's adverse effect on the boundary layer. A full span bump (upper surface aerofoil shape) model mounted on the floor of a transonic wind tunnel was previously tested with several configurations of such shock-bump roughness. This study performed steady Navier-Stokes CFD analysis of the working section flow to match the experimental data for the smooth surface bump, and then to assess the affect of simulated shock bump roughness. The performance of several turbulence models was compared with experimental data (Mach 0.55 inflow, Reynolds number based on bump chord between 3.1 - 3.6 million) - the $\kappa-\omega$ SST model being found to be the most accurate for this type of problem. It was predicted that shock-bump roughness tends to move the shock wave downstream and reduce its strength in cases where the roughness elements are located directly under the interaction, as in the solid shock bump case. This suggests that the virtual displacement effect of surface roughness can be designed to provide the same shock-bump effect as a solid protuberance but potentially without the extra weight and pressure drag. Shock-bump roughness arranged in strips aligned with the streamwise flow were predicted to perform better than those arranged at a 30 degree skew angle to the flow. No conclusive evidence from the numerical models shows that shock-bump roughness can improve the separated flows if placed upstream of the shock, in cases where the shock wave moved downstream of the roughness location.

I. Nomenclature

c	=	Bump-chord length (m)
F_N	=	Normal force on the bump (N)
F_X	=	Axial force on the bump (N)
C_p	=	Pressure coefficient
C_s	=	Roughness constant
d	=	Distance between the roughness strip (mm)
G	=	Geometric growth ratio
k	=	Turbulent kinetic energy (J/kg)
k_s	=	Equivalent sand grain roughness height (μm)
k_s^+	=	Non-dimensional roughness height
M	=	Mach Number

*Visiting Researcher at the School of Aerospace, Transport & Manufacturing, Cranfield University, UK
†Lecturer in Aerodynamics, School of Aerospace, Transport & Manufacturing, Cranfield University,UK, AIAA member.
‡Professor in Aerodynamics, School of Aerospace, Transport & Manufacturing, Cranfield University, UK, Senior AIAA Member.
§Aerodynamic Engineer, Safran AE, Théhillac, Brittany, France.

Published by AIAA. This is the Author Accepted Manuscript issued with: Creative Commons Attribution Non-Commercial License (CC:BY:NC 4.0).
The final published version (version of record) is available online at DOI:10.2514/6.2024-2723. Please refer to any applicable publisher terms of use.

P_{in} = Inlet pressure (Pa)
P_{out} = Outlet pressure (Pa)
P_r = Pressure ratio
Re = Reynolds Number
u = Velocity in the x direction (m/s)
u^+ = Non-dimensional velocity in the x direction
u_τ = Friction velocity (m/s)
y^+ = Non-dimensional distance from the wall
λ = Width of each roughness strip (mm)
ϕ = Angle between the roughness strip axis and freestream velocity direction (degrees)

II. Introduction

Since the invention of the jet engine, almost all commercial transports now cruise at transonic speed, in order to increase the aircraft's range and efficiency. Leading edge sweep and supercritical aerofoil sections are employed to delay transonic drag rise and the formation of weak shocks on the wing surfaces. Aircraft performance is limited by the strengthening of these shock waves as cruise Mach number and wing angle of attack are increased, which will cause boundary layer separation - called shock induced boundary layer separation. The boundary layer tends to dissipate the sharp pressure rise across a weak shock wave and can remain attached to the surface if the shock is not too strong. The shock waves lead to a rapid increase in drag, both due to the additional loss of total pressure (wave drag) and also because the pressure rise through a shock wave thickens the boundary layer, leading to increased viscous drag. Transonic shock buffet is a phenomenon where an interaction between shock waves and the separated shear-layer leads to a self-sustained periodic shock motion that in turn involves large fluctuations of wing loading [1]. Buffet gradually develops over a wing as its incidence rises, compromising passenger comfort, structural fatigue and potentially leading to wing structural collapse [2, 3]. This phenomena severely limits the flight envelopes of aircraft calling for airworthiness regulations to set requirements on a sufficient margin before onset, in both flight Mach number and angle of attack. Safety is the single most important principle in aviation, and ACARE regulations require design for less than 1 accident for each ten million commercial flights in Europe. This means that buffet suppression technology is of critical importance. Much research has been devoted to understanding and delaying this unsteady regime and numerous flow control techniques, both active [4–6] and passive. One particular passive control technique found to be successful in laboratory transonic flows has been shock bumps [7–9]. These are designed to sit under the shock interaction mimicking the displacement effect of a separation bubble, thereby creating a lambda shock wave bifurcation which is known to reduce the local total pressure loss through the shock system and reduce the associated pressure gradient. However, shock bumps create their own protuberance pressure drag which can offset the wave drag reduction, and therefore have to be carefully designed with spanwise periodicity to maximise performance. The idea of using enhanced boundary layer displacement effect by implementing sub-boundary layer scale distributed roughness to create the same effect was tested by [10] and [11]. This study follows on from this latter work, which reported on an entirely experimental investigation to test this passive technique on a wind tunnel wall bump model which simulated the flow over the upper surface of an aerofoil. The surface pressure distribution data and corresponding shadowgraph flow visualisation, showed that such periodic roughness can bifurcate the shock wave and delay shock-induced separations, depending on the orientation (strips in line with or at 30 degree skew angle to the freestream flow) of the roughness and its periodicity (width of the roughness strips and the spanwise gap between them). In particular this study aimed to use steady Navier-Stokes CFD analysis of the working section flow to match the experimental data for the smooth surface bump, and then to assess the affect of shock bump roughness by numerical modelling.

III. Test Case

The experimental results reported in [11] were obtained from an experimental campaign at the City University of London's T5 Transonic closed return Wind tunnel, shown in Fig. 1,which is part of the UK's National Wind Tunnel Facility. The test section has the dimensions 0.2m x 0.25m x 0.5m and can operate in the Mach number range of 0.5-1.6.



Fig. 1 Transonic Wind Tunnel with model mounted at City University of London, UK.

The bump model had a 14% t/c ratio, and a chord of 309.55mm with a maximum height of 43mm. 10mm roughness strips were placed on the top of a removable block embedded into the bump model, whose top surface followed the bump profile. The strips were located between x=94mm and 147.5mm from the leading edge of the bump, as shown in Fig. 2. This location was chosen as this was known to be where the shock wave was situated for the flow condition corresponding with the typical cruise condition. For all the cases, ballotini roughness of average height of 500µm was used. Several configurations of distributed surface roughness were tested. The spacing between the strips as well as the angle of the strips varied according to the details in Table 1. Here λ is the width of the roughness strips, ϕ is the skew angle of the strips relative to the streamwise, and k_s is the roughness height, and d is the spacing between the roughness strip.

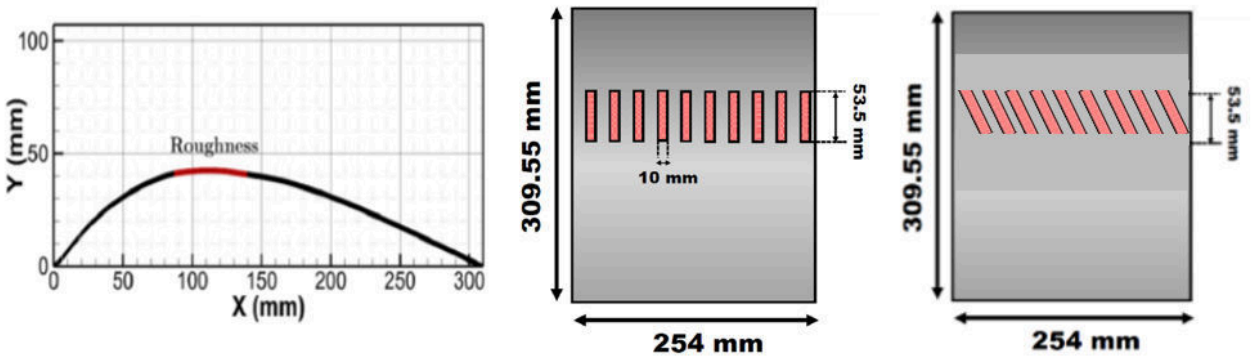


Fig. 2 Bump geometry and roughness strip configurations.

Table 1 *Details of the roughness strips used in the experiment*

ϕ (°)	λ (mm)	k_s (µm)	d (mm)
0	**10**	**500**	**5**
0	**10**	**500**	**10**
30	**10**	**500**	**5**
30	**10**	**500**	**10**

The experimental measurements included chord-wise surface pressure on the bump surface located on the centre-span axis. Mercury pressure gauges were used at the front of the bump (before the roughness) where the flow was choked, and piezo-electric dynamic pressure sensors at the back (after the roughness), where the flow was most likely to change with changing back pressure. No pressure measurement stations were placed where the roughness strips were located.

The wind tunnel is a closed return ejector type where 600 psi is stored in a reservoir which fed the four injectors, located downstream of the working section. The injection pressure was controlled by valves, and the resulting jets entrained the air in the diffuser to drive the circulation in the tunnel. The higher the blowing pressure, the higher the acceleration around the bump model, and the further rearward the shock location. The ejector blowing pressure valve was set manually and indicated via an analogue display in units of pounds per square inch (PSI). Details of the experimental arrangements and procedures are given in reference [11]. Pressure readings on the manometer were captured once the pressure distribution stabilized, while the pressure measurements on the rear of the model surface were acquired at 3kHz over the last 5 seconds of the 15 seconds of wind tunnel run. These data were then averaged over time to obtain a single value for each pressure tap. This procedure was applied for each configuration with 8 different ejector pressure settings (15, 20, 25, 30, 35, 40, 45 and 50 PSI). A minimum of two sets of measurements were made for each blowing pressure for repeatability check.

The experimentally measured surface pressure data is presented in Fig. 3 for the smooth surface case, in terms of pressure ratio (the ratio of local static pressure over the total pressure). The plot indicates the pressure ratio corresponding to the sonic condition to indicate the region of supersonic flow for each case, together with the bump geometry and the location of each pressure sensor.

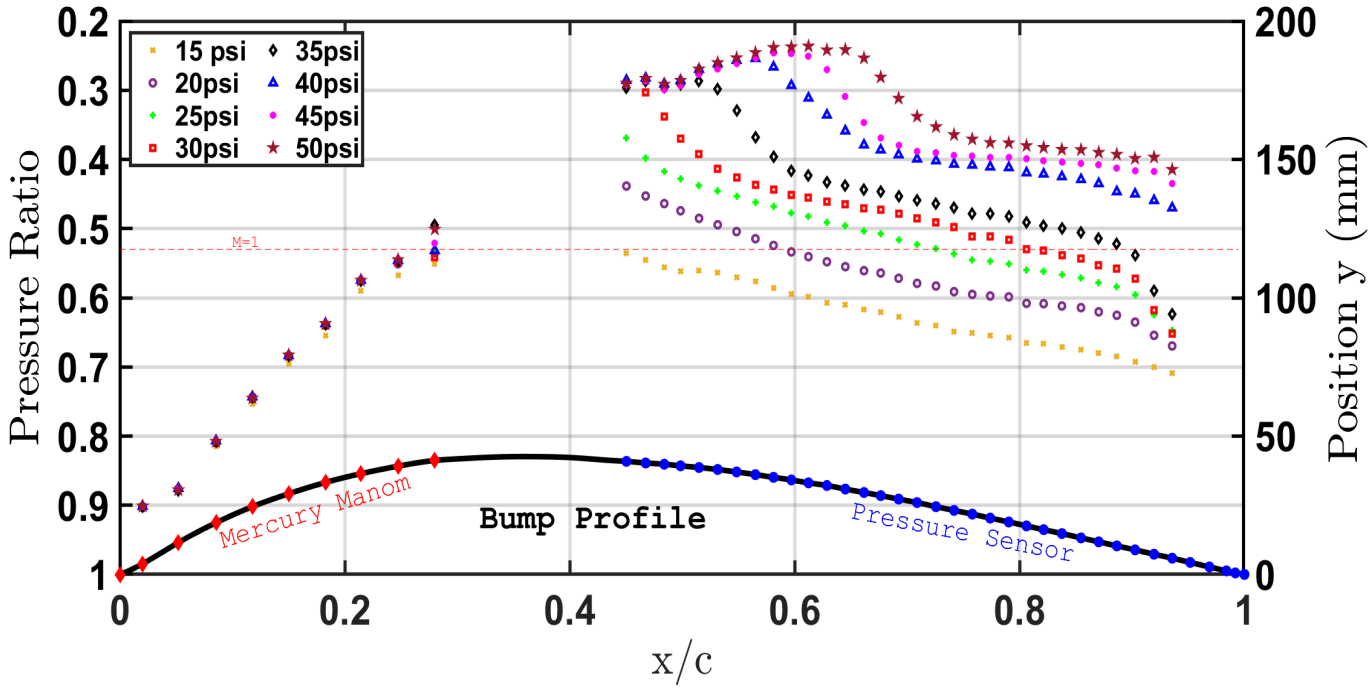


Fig. 3 Evolution of the measured pressure ratio distribution for the different ejector blowing pressures.

The pressure distribution up to x/c of 0.28 remains almost constant as this region of the tunnel flow is choked by the supersonic flow over the crest of the bump. The flow then enters the region of adverse pressure gradient towards the end of the bump and the supersonic flow is terminated by a shock wave and decelerated to subsonic speed. At the high ejector blowing pressures (above 35 PSI) the shock wave becomes so strong that it begins to separate the boundary layer, indicated by the pressure plateau behind the shock. The associated shadowgraph photographs taken during the experiment will not be compared in this paper.

A. Computational Analysis

This study employed the commercial CFD package ANSYS FLUENT to carry out CFD simulations on the bump encompassing the geometry of the working section of the wind tunnel in an effort to capture the 3D nature of the flow. The dimensions of the computational domain were 1.368m x 0.206m x 0.254m respectively, as shown in Fig. 4

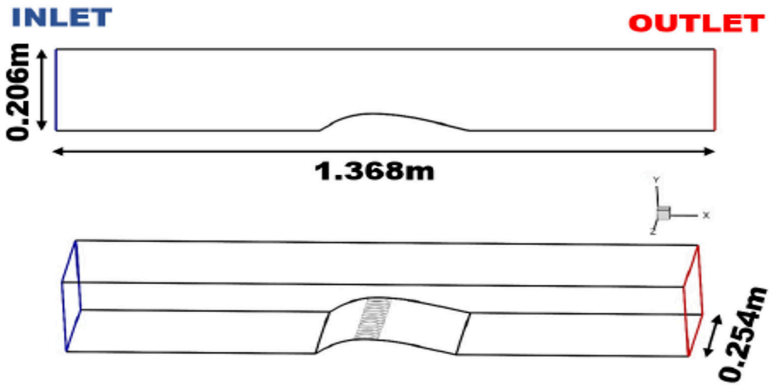


Fig. 4 Bump geometry and roughness strip configurations.

The bump points were interpolated using the curve fitting tool on MATLAB to ensure a smooth bump curve was created. This helps in getting rid of any erroneous static pressure disturbances predicted on the surface of the bump due to discontinuities in the computational surface curvature.

A base level 3D structured mesh was created for the smooth case (without roughness) encompassing 15.4 million cells in three distinct parts: the upstream volume, the bump volume and the downstream volume as shown in Fig. 5

The axial cell size reduced from the inlet and the outlet towards the bump, such that the greatest mesh resolution was focused on the bump where the highest flow gradients occurred. Cells were also focussed on the crest area of the bump and the immediate downstream region where the shock wave was found to occur in the experiments. In addition cells were clustered towards each of the four tunnel walls so as to properly resolve the boundary layers, sufficient for a value of y+ at the wall of order 1 everywhere.

A mesh independence study was performed to ensure mesh independent results for the surface pressure and flow structure. Four meshes were generated, the coarsest of 8 million cells, and the finest being of 24 million cells, and the flow case corresponding to 50 PSI blowing pressure - the most extreme case with separated flow - was computed using the $\kappa - \omega$ SST turbulence model, prior to a comprehensive assessment of the most appropriate model.

The computations solved the steady Reynolds-averaged Navier-Stokes equations. An upwind Roe flux difference splitting method with a second-order scheme was used to resolve the inviscid fluxes. The diffusive fluxes are treated using the second-order central differencing method. A no-slip boundary condition was applied to all four walls while the inlet boundary condition set the inlet pressure, temperature and Mach number to the experimental values:

$P_{in} = 82,400Pa$
$T_{in} = 270K$
$M_{in} = 0.55$

The process of identifying the correct outlet boundary condition is described later in the paper, but an outlet pressure ratio of 0.73 was employed, which was the value found from this study.

Fig. 6 presents the comparison of the resulting predicted pressure distributions from the 4 meshes for this case. Here, x/c is the distance along the bump divided by the chord length (0.309m). The pressure is normalised by dividing it with the inlet total pressure (101330Pa). The comparison shows that the 8 million elements mesh failed to accurately capture the shock location. The 15, 20, and 24 million elements mesh performed much better in resolving the shock position and strength, with pressures resolved to within 5% of the actual experimental results. It was decided that an analysis of the predicted normal force on the bump F_N and the corresponding axial force F_X would be of interest, where the ratio F_N/F_X would be a figure of merit for aerodynamic efficiency - the higher the better. This analysis shows that

the predicted force ratio is very close for the three finest meshes, and it was decided to take the 15 million cell mesh as providing mesh converged solutions. It was therefore this mesh that was used for the rest of the smooth case calculations.

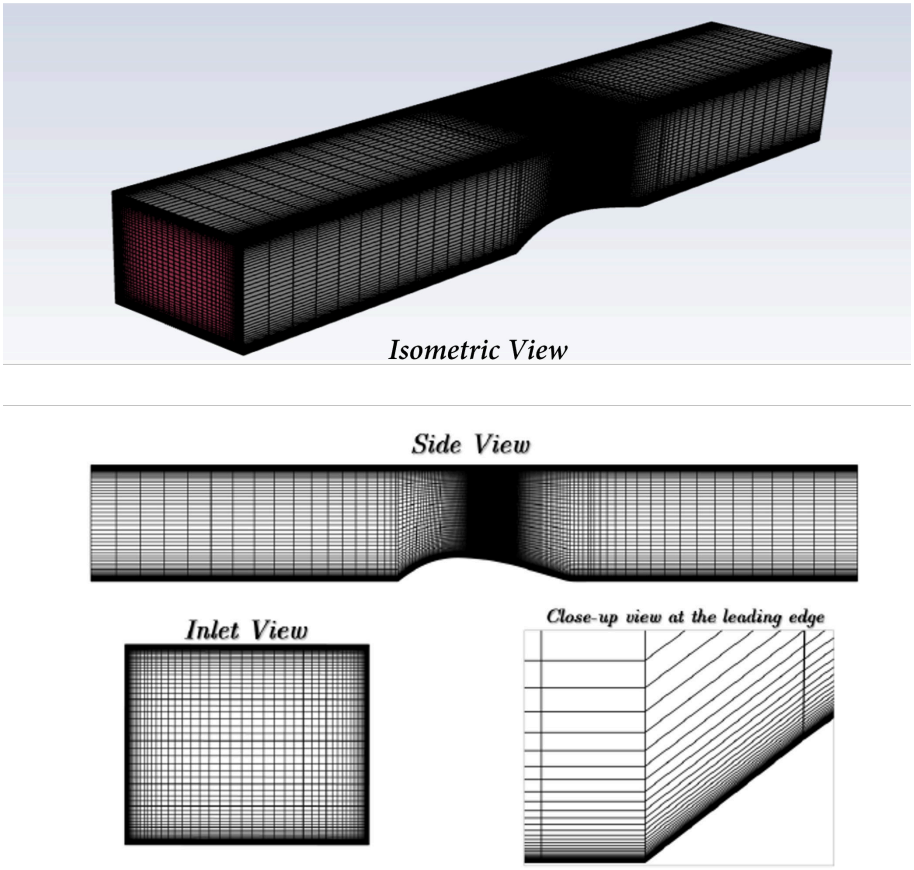


Fig. 5 Bump geometry and roughness strip configurations.

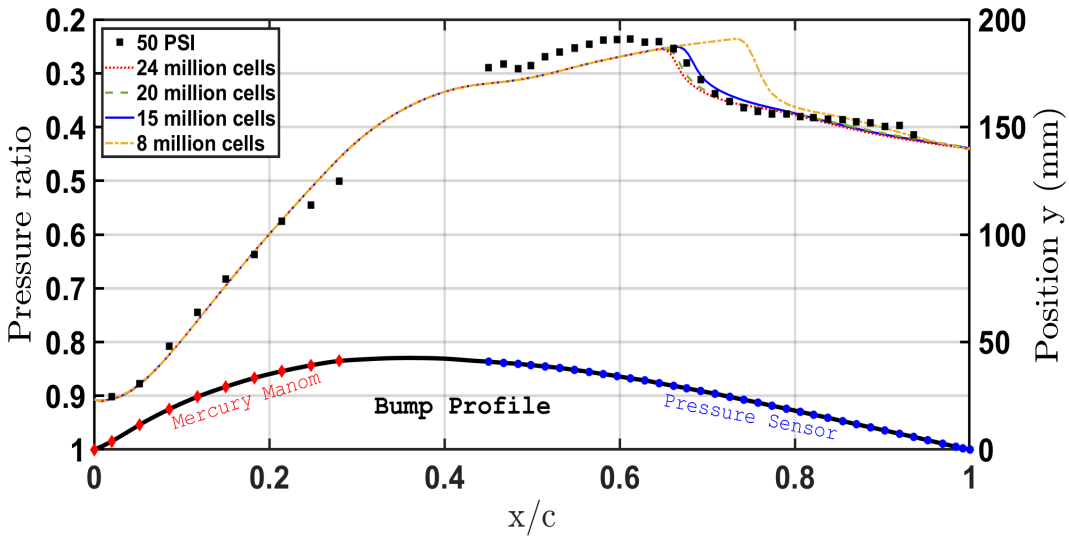


Fig. 6 Comparison surface pressure predictions from the 4 meshes against the experimental results.

Table 2 *Maximum error % in predicted pressure and predicted forces for the 4 meshes*

Mesh cell count	Max % error in pressure	F_N (N)	F_X (N)	F_N/F_X
8 million	13.1%	2912.67	456.54	6.38
15 million	4.3%	2841.06	436.80	6.50
20 million	3.8%	2830.09	434.13	6.52
24 million	4.5%	2820.24	431.66	6.53

The flow Mach number ahead of the bump was maintained constant at M=0.55, for all ejector blowing cases corresponding with the experimental working section entry condition. A first set of calculations was performed for the smooth surface bump case in order to "tune" the CFD model to identify the correct boundary conditions, turbulence model, and mesh requirements to reproduce the experimental data. A first guess was made for the outlet pressure ratio, being the last value recorded at the most rear station in the experimental data. Solutions were then generated, in increments of pressure ratio of 0.02, using the $\kappa - \omega$ SST turbulence model to identify that outlet pressure ratio which provided the closest match with the experimental data for each case. The equality of total temperature across a shock wave, and the isotropic relation was used to calculate the corresponding value of outlet temperature.

The Reynolds number based on bump chord was in the range of 3.1 to 3.6 million, and so it was confidently assumed that the flow was fully turbulent. The 50 PSI ejector blowing case was again used as the basis for the turbulence model assessment. A number of turbulence models were used to compute this flow. Fig. 7 presents the comparison between the experimentally measure surface pressure data with the corresponding predictions from the best three turbulence models. It can clearly be seen that the $\kappa - \omega$ SST turbulence model was superior in capturing the shock location, its strength and the subsequent surface pressures under the separated flow region. This is in accord with previous findings in the literature which shows that this turbulence model is particularly effective in resolving transonic separated flows. Table 3 presents the figures for the maximum error between the experimentally measured and predicted surface pressure anywhere on the bump.

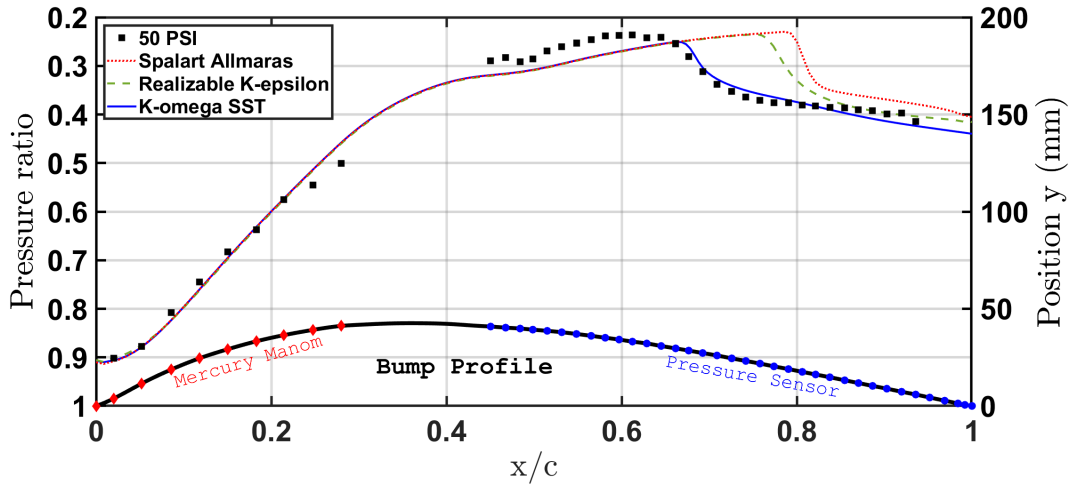


Fig. 7 Comparison of the surface pressure distributions predicted by the 3 best turbulence models for the 50psi ejector blowing case.

Table 3 *Maximum % error in surface pressure for the three best turbulence model cases*

Turbulence Model	Max % error in pressure
$\kappa - \omega$ SST	4.3%
$\kappa - \epsilon$ Realizable	17.1%
Spalart Allmaras	23.5%

For completeness, Table 4 summarizes the relationship between the ejector blowing pressures and the tunnel working section exit pressure used in the CFD analysis that provides the best match with the experimental data in terms of shock location, strength and the lowest maximum error between the experimentally measured surface pressure and the CFD predicted values.

Table 4 *Minimum error between pressure ratio and blowing pressure for pressure distribution*

Blowing Pressure (PSI)	**Pressure ratio with the least error**	**Relative error (%)**
15	**0.93**	**1.9**
20	**0.88**	**3.7**
25	**0.85**	**7.4**
30	**0.83**	**7.5**
35	**0.81**	**11.6**
40	**0.77**	**6.1**
45	**0.76**	**6.2**
50	**0.73**	**4.3**

A different meshing approach had to be employed for the shock bump roughness cases, as a structured mesh would have been over-complicated and excessive in cell requirement to properly capture the topology of the roughness strip configurations, particularly for the 30 degree skewed strips. A hybrid unstructured meshing approach was therefore used for the shock bump roughness cases. The roughness strips on the bump were created at CAD level. All the meshes were composed of prismatic cells around the surface of the aerofoil and around each wind tunnel wall, in order to correctly resolve the boundary layers, with unstructured tetrahedron cells in the interior of the domain.

A mesh sensitivity study was performed, for the smooth surface 15 PSI and the 50 PSI ejector blowing cases, where no roughness boundary condition was applied to the strip surfaces, to identify the cell count and cell distributions required to match the results of the structured mesh cases, to within 2 percent for the shock location / strength and pressure level across the bump. A mesh of 19 million cells was found to provide this match with the structured cell results, details of which are presented in Fig. 8.

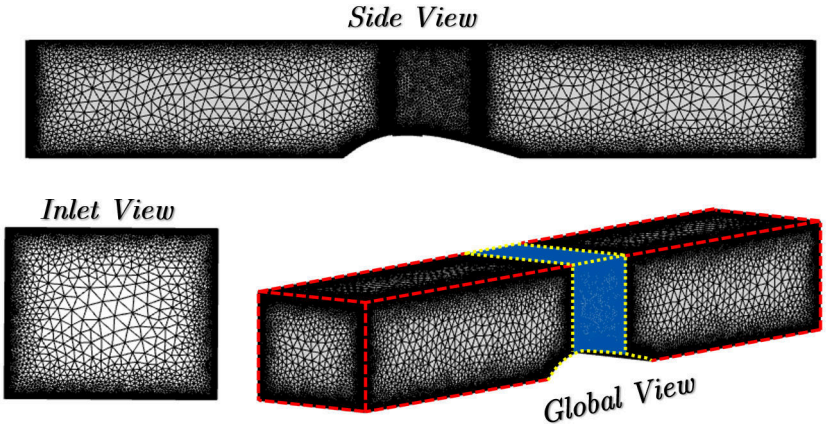


Fig. 8 Details of the 19 million cell unstructured mesh for the 0 degree skew shock-bump roughness case

The numerical method employed to model the effect of the distributed roughness applied to the strips is derived from the method of Nikuradse [12]. The method is semi-empirical, making use of experimental data and characterizes the effect of the roughness by its location, density and height. Uniform grain type roughness was assumed in the CFD calculations and was numerically modelled using a wall no slip condition and adding a roughness height (k_s) and a roughness constant (C_s). The chosen value for k_s was 500µm as the one applied during the experiment, and the chosen value for C_s was 0.5, which indicates uniform roughness, as represented in Fig. 9,

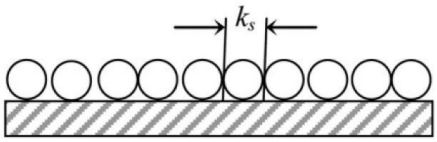


Fig. 9 Representation of surface roughness using the Nikuradse sand grain analogy

IV. Results and Discussion

The comparison between the experimentally measured and numerically predicted surface pressure distributions, using the structured mesh, is presented in Fig. 10. The pressure drop on the forward face of the bump is seen to be resolved very well almost up to the start of the bump. The discrepancy here is almost certainly associated with the surface discontinuity between the main model section and the insert on which the roughness strips were attached. The discrepancy between the predicted trend and the experimental data immediately after the insert, where the suction is under-predicted by the CFD method, may well also be due to this model manufacturing issue. However, the overall trend in the movement of the shock downstream with ejector blowing pressure, and gradual dissipation of the shock strength is resolved. The precise location of the shock wave, particularly the location of the shock foot (that is the first occurrence of pressure rise) is not well captured for ejector pressure ratios lower than 45 PSI, with a spacial error of up to $\Delta x/c$ of 0.05.

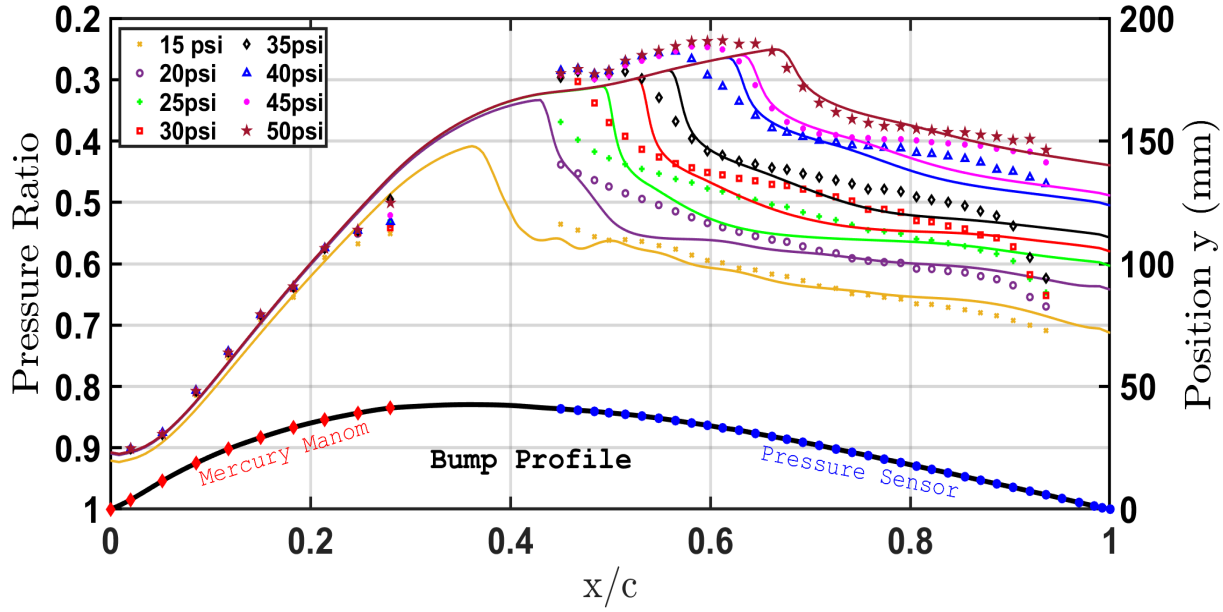


Fig. 10 Comparison of experimentally measured and CFD predicted surface pressure distributions for different tunnel ejector blowing pressures.

The trend in the progressive reduction in post shock surface pressure with increasing ejector blowing pressure is also successfully captured, though the discrepancy is as high as 15 percent close to the shock in some cases. In general, the physical trends are captured well enough by the CFD model developed in this study to allow for a numerical

assessment of the effect of the surface roughness on this baseline flow. The rest of this analysis therefore focuses on purely comparative assessment of the CFD data. Comparison with experimental data for the roughness cases requires further processing of the measured data and will appear in a later paper.

The CAD models for the roughness cases and the relative meshes were built for 3 different roughness cases - designated 10mm0degree, 20mm0degree, and 5mm30degree, where the first term is the spanwise gap distance between strips (in millimeters) and the second term is the angle between the roughness strip axis and the freestream flow direction (x-axis) in degrees.

Steady Navier-Stokes simulations using the $k-\omega$ SST turbulence model, at 4 different blowing pressures were run for the smooth bump and the three roughness cases. The Mach number contours on the centre-span x-y plane as well as the centre span pressure distribution on the bump are presented in figures 11, 12, 13, and 14.

For the $P_r = 0.93$ case, a nearly normal shock appears in the vicinity of x/c=40% for the smooth case. From the pressure distribution on the bump, it can be seen that the shock bump roughness elements tend to move the shock downstream significantly in all three cases. For the 5mm30degree and 10mm0degree cases, it can be observed that the shock is also weaker, in terms of the change in pressure across it, than in the smooth surface case. The Mach number contours on the spanwise centreplane show that the shock waves sit above the shock-bump roughness elements and result in a downstream movement of the shock and a large extent of supersonic flow (the orange/red region), indicating an enhanced extent of surface suction. This is particularly the case for the 20mm0degree case. The shock-bump roughness does not appear to have affected significantly the predicted boundary layer thickening at the rear of the bump. Table 5 presents the predicted normal force and axial force components on the bump for the 0.93 tunnel pressure ratio case, together with the breakdown of the axial force into its pressure and friction components. All of the shock-bump roughness cases are predicted to increase the normal force and reduce the axial force on the bump, resulting in up to 5 percent increase in the normal to axial force ratio. Breakdown of axial force predictions shows that while the the pressure contribution is reduced by the shock-bump roughness, by a maximum of 3 percent, the friction contribution is increased by up to 5 percent.

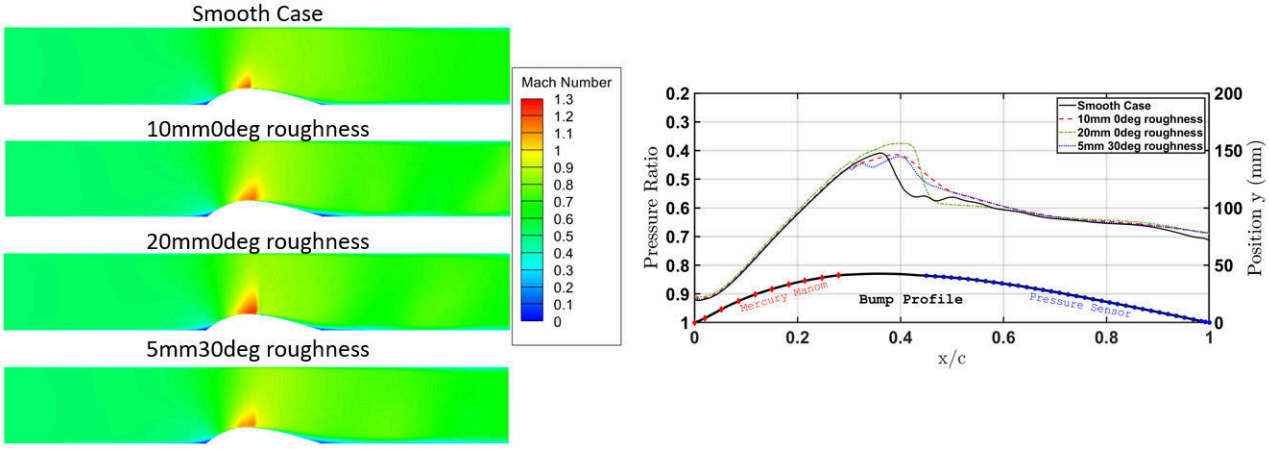


Fig. 11 Centre-span plane Mach number contours and corresponding surface pressure distribution for Pressure ratio of 0.93

Table 5 *Averaged Axial and Normal Forces for the 4 cases ($P_r = 0.93$)*

Roughness Case	F_N (N)	F_X (N)	F_X (pressure contribution) (N)	F_X (viscous contribution) (N)	F_N/F_X
No Roughness	1372.73	156.43	152.20	4.23	8.77
10mm 0degrees	1416.85	154.72	150.27	4.45	9.16
20mm 0degrees	1418.47	153.51	149.05	4.46	9.24
5mm 30degrees	1389.01	152.27	147.99	4.28	9.12

From this analysis, the shock-bump roughness is predicted to behave exactly as their solid counterparts are meant to

behave, and preliminary assessment of the experimental data matches this finding. If the detailed assessment of the measured data confirms this, then use of distributed roughness strips which are much easier to apply as a retrofit, may be a practical alternative to solid protuberance shock-bumps for shock control and buffet suppression.

For the $P_r = 0.85$, case, the predicted shock waves for all cases are seen to have moved downstream of the shock bump roughness elements, which will therefore not be performing as designed. In fact this is the same as all the pressure ratio cases at or below 0.85, which can be regarded as off-design cases. The predicted surface pressure distributions suggest that the zero degree roughness strip configurations move the shockwave a small distance downstream, but the roughness strips at 30 degree skew move the shock wave upstream. The Mach number contour plots clearly show that this latter configuration is predicted to spoil the flow by fixing a shock-induced separation, while the zero skew roughness strips do not significantly change the flow-field from that seen in the smooth case. It should be noted that the solution of the 5mm30deg case could not be fully converged, indicating that this flow is probably likely to be unsteady in reality. The Mach contour plot for this flow is for a quasi-time iteration at which the flow was separated. At other iterations the flow was attached. At this tunnel pressure ratio, where the shock wave is only slightly downstream of the roughness strips, the zero degree elements are therefore predicted to have a marginally beneficial effect, while the 30 degree configuration is predicted to spoil the flow.

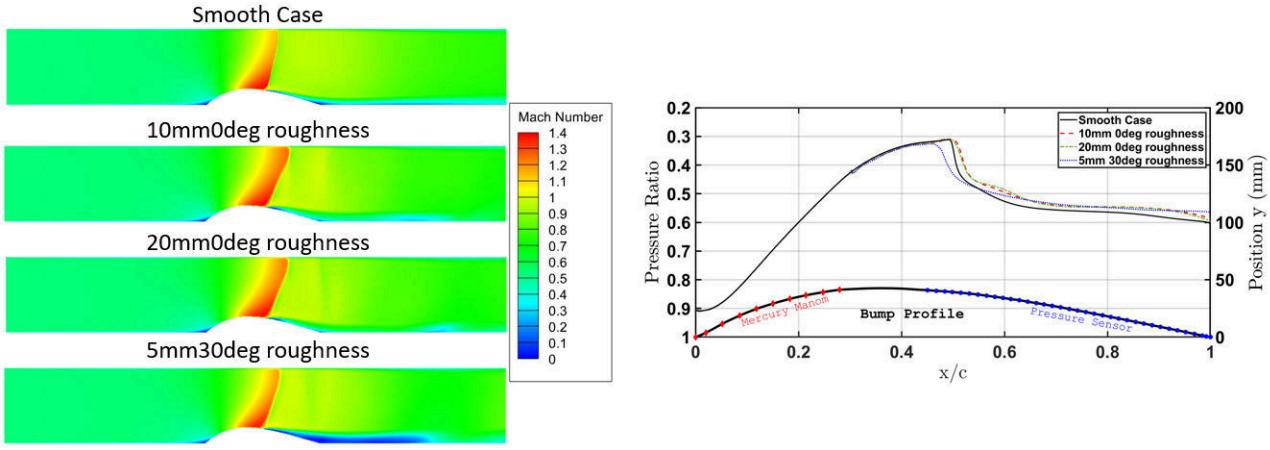


Fig. 12 Centre-span plane Mach number contours and corresponding surface pressure distribution for Pressure ratio of 0.85

Table 6 indicates that while the zero degree roughness configurations are predicted to increase the normal force on the bump, they will also increase the axial force, leading to a small drop in normal to axial force ratio - a marginally detrimental effect in aerodynamic efficiency. The 30 degree roughness configuration was predicted to actually increase the normal force but also reduce the axial force component, also resulting in a small reduction in the force ratio. Scrutiny of the figures for axial force broken down into its pressure and friction contributions reveals that the roughness, in all three cases, increases both the pressure and friction component, with the friction component increasing by as much as 30 percent.

Table 6 *Averaged Axial and Normal Forces for the 4 cases ($P_r = 0.85$)*

Roughness Case	F_N (N)	F_X (N)	F_X (pressure contribution) (N)	F_X (viscous contribution) (N)	F_N/F_X
No Roughness	2026.03	248.96	244.44	4.52	8.14
10mm 0degrees	2113.88	267.80	261.95	5.85	7.89
20mm 0degrees	2113.01	266.78	261.43	5.35	7.92
5mm 30degrees	2061.08	257.44	251.87	5.57	8.01

The flow topology for the $P_r = 0.83$ case is predicted to be very similar to that seen for the $P_r = 0.85$ case. The

solution for the 5mm30degree case was also found not to completely converge, oscillating over several hundred iterations between an attached flow and a rear shock induced separated case much like that depicted in figure 12. Again, this would indicate that the real flow is likely to be unsteady for this 30 degree skew roughness strip case. Here there is also evidence that the effect of zero degree skewed shock-bump roughness upstream of the shock is to reduce the thickness of the bottom wall boundary layer downstream of the bump. The corresponding surface pressure comparison for this tunnel pressure ratio again shows a predicted downstream movement of the shock wave with the addition of shock-bump roughness upstream, the best result achieved with the zero degree skew strips. Looking at the breakdown of forces on the bump for this case, presented in table 7 shows that the predicted effect of the shock-bump roughness is a 5 - 6 percent increase in normal force, but a 8 - 10 percent increase in axial force, resulting in an overall loss of aerodynamic efficiency measured by the normal to axial force ratio. The rise in axial force is predicted to come from a rise in both pressure and friction components of this force.

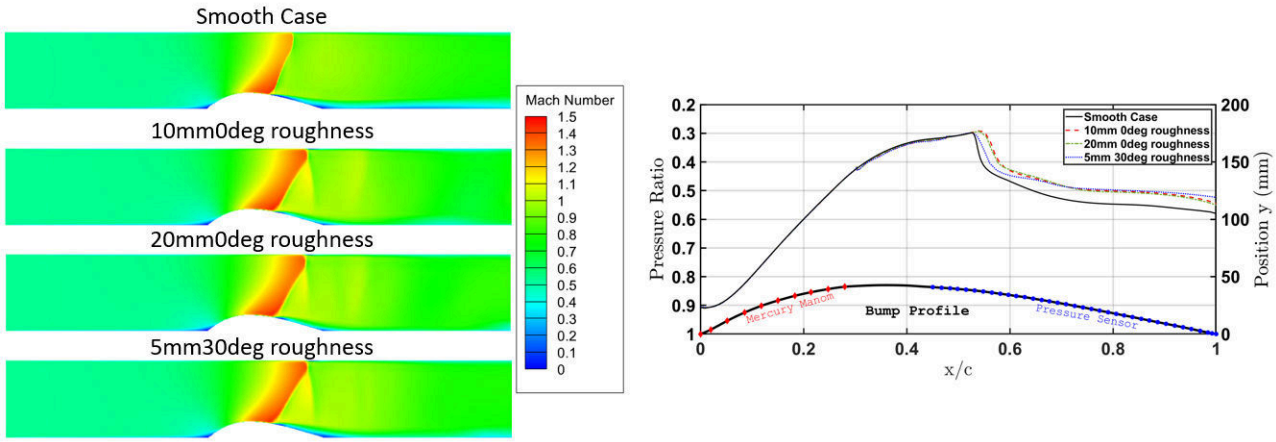


Fig. 13 Centre-span plane Mach number contours and corresponding surface pressure distribution for Pressure ratio of 0.83

Table 7 *Averaged Axial and Normal Forces for the 4 cases (P_r = 0.83)*

Roughness Case	F_N (N)	F_X (N)	F_X (pressure contribution) (N)	F_X (viscous contribution) (N)	F_N/F_X
No Roughness	2181.78	280.45	275.73	4.72	7.78
10mm 0degrees	2292.38	305.71	299.55	6.16	7.49
20mm 0degrees	2320.29	303.75	298.17	5.57	7.63
5mm 30degrees	2300.45	308.03	301.76	6.26	7.47

For the 0.77 tunnel pressure ratio case the predicted Mach number contour plots on the centre plane shows that the baseline smooth surface flow has a shock-induced separation on the rear surface, with a shock interaction and separated boundary layer on the top wall as well, together with secondary weaker shocks downstream. The flow structure for all three shock-bump roughness cases are generally equivalent, showing that these features no longer significantly improve the baseline flow. Interestingly, both zero skew roughness strip cases predict a considerably healthier, thinner lower wall boundary layer far downstream of the bump, compared with the baseline smooth case. The corresponding surface pressure comparisons show that the zero degree shock-bump roughness cases do not change the position of shock formation, and if anything slightly increase the shock strength. The 30 degree skewed roughness case, however, actually spoils the flow, shifting the shock wave by about 5 percent upstream. The predicted forces acting on the bump, plotted in table 8, show that all roughness configurations increase the normal force, but also the axial force components, resulting in insignificant changes to the force ratio. Scrutiny of the breakdown of the computed axial forces shows that while the there is no significant change in pressure contribution the friction contribution reduces by up to 26 percent. This is due the large extent of the separated flow on the rear bump with low velocity reversed flow above the surface.

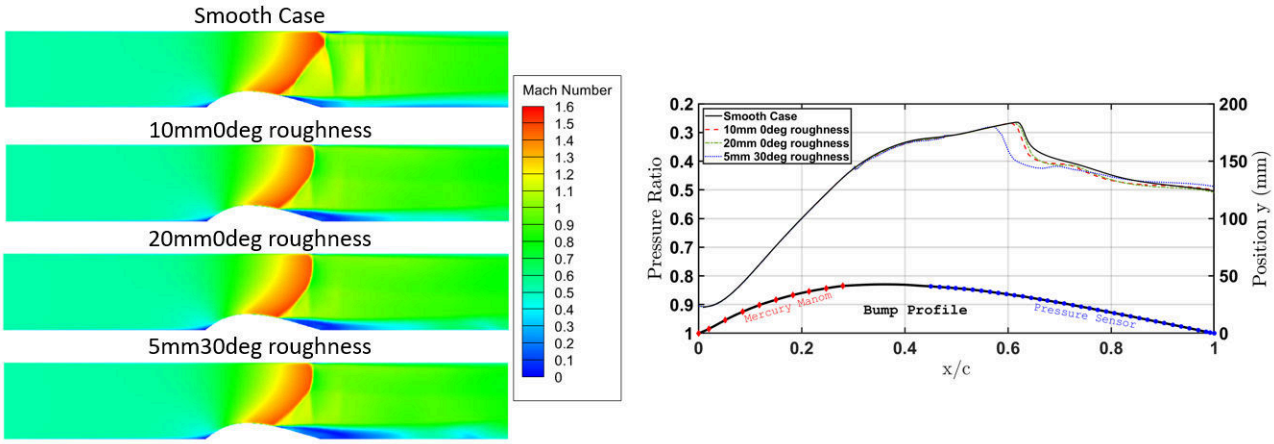


Fig. 14 Centre-span plane Mach number contours and corresponding surface pressure distribution for Pressure ratio of 0.77

Table 8 *Averaged Axial and Normal Forces for the 4 cases (P_r = 0.77)*

Roughness Case	F_N (N)	F_X (N)	F_X (pressure contribution) (N)	F_X (viscous contribution) (N)	F_N/F_X
No Roughness	2610.06	377.38	371.89	5.49	6.91
10mm 0degrees	2585.01	372.76	368.44	4.31	6.93
20mm 0degrees	2589.02	372.61	367.97	4.63	6.95
5mm 30degrees	2580.8	372.03	368.01	4.03	6.94

V. Conclusions

The results of this study clearly shows that detailed Reynolds Averaged Navier-Stokes analysis, with distributed surface roughness effects modelled using the Nikuradse approach, predicts that shock-bump roughness strips have a significant effect on the flowfield around a wall mounted bump in transonic flow. In particular the analysis suggests that shock bump roughness strips, when positioned directly underneath the shock interaction, behaves in the same manner as that measured and predicted in the literature as solid shock-bumps. They move the shock wave downstream, extending the interaction but reducing the shock strength and, thereby, the axial force, akin to the drag for a full aerofoil geometry. The overall aerodynamic efficiency, as defined by the ratio of normal force to axial force was also predicted to increase by up to 5 percent. The most effective configuration of roughness strips was found to be inline with the freestream flow rather than set at 30 degrees skew. For off design cases, where the shock wave moves downstream beyond the shock-bump roughness location, the effect of these devices was predicted to be less beneficial overall, but the zero degree skew configurations of shock-roughness were predicted to still move the shock more rearward compared with the corresponding smooth surface case. In general the aerodynamic efficiency reduced slightly in off-design condition, due mostly to a reduction in normal force, compared with the smooth surface case. This study has demonstrated that there is potential in the practical application of shock-bump roughness for shock wave control and possibly buffet onset suppression, but this will ultimately need to be experimentally assessed on a full aerofoil configuration in transonic flow, which includes the effect of circulation which is not present in the flow investigated in this study.

References

[1] Lee, B.H.K. "Self-sustained shock oscillations on airfoils at transonic speeds". *Prog. Aerosp. Sci.* 2001, *37*, 147–196.

[2] Mayer, R. Lutz, T. Kräme, E. and Dandois, J. "Control of Transonic Buffet by Shock Control Bumps on Wing-Body Configuration". *J. of Aircraft* 2019, *56*, 556–568.

[3] Geoghegan, J. Giannelis, N. and Vio, G. "A Numerical Investigation of the Geometric Parametrisation of Shock Control Bumps for Transonic Shock Oscillation Control". *Journal of Fluids* 2020, *10*, 556-568.

[4] Caruana, D. Mignosi, A. Corrège, M. Le Pourhiet, A. Rodde, A.M. "Buffet and buffeting control in transonic flow". *Aerosp. Sci. Technol.* 2005, *9*, 605–616.

[5] Gao, C. Zhang, W. Ye, Z. "Numerical study on closed-loop control of transonic buffet suppression by trailing edge flap". *Comput. Fluids*, 2016, *132*, 32–45.

[6] Dandois, J. Lepage, A. Dor, J.-B. Molton, P. Ternoy, F. Geeraert, A. Brunet, V. Coustols, É. "Open and Closed-Loop Control of Transonic Buffet on 3D Turbulent Wings Using Fluidic Devices". *Comptes Rendus Mec.* 2014, *342*, 425–436.

[7] Eastwood, J.P. Jarrett, J.P. "Toward Designing with Three-Dimensional Bumps for Lift/Drag Improvement and Buffet Alleviation". *AIAA Journal*, 2012, *50*, 2882–2898.

[8] Rybalko, M.; Babinsky, H.; Loth, E. "Vortex Generators for a Normal Shock/Boundary Layer Interaction with a Downstream Diffuser". *J. Propuls. Power* 2012, *28*, 71–82.

[9] Mayer, R. Lutz, T. Krämer, E. "Numerical Study on the Ability of Shock Control Bumps for Buffet Control". *AIAA Journal*, 2018, *56*, 1978–1987.

[10] Dietz, G. "Passive Shock Control Concept for Drag Reduction in Transonic Flow". *J. of Aircraft*, 2005, *42*, 794–798.

[11] Di Pasquale, D., Prince, S. "Passive Transonic Shock Control on Bump Flow for Wing Buffet Suppression". *Aerospace*, 2023, *10*, 569.

[12] Nikuradse, J.m "Laws of flows in rough pipes" *Technical Memorandum*, 1937, *129*.



https://dspace.org/

CFD study of shock bump roughness for transonic shock control and buffet alleviation

Di Pasquale, Davide

2024-01-04
American Institute of Aeronautics and Astronautics (AIAA)
https://doi.org/10.2514/6.2024-2723
Di Pasquale D. (2024) CFD study of shock bump roughness for transonic shock control and buffet alleviation. In: AIAA SCITECH 2024 Forum, 8-12 January 2024, Orlando, USA. Paper number AIAA 2024-2723

Downloaded from a DSpace repository. https://dspace.org/